

Interferometric visibility of single-lens models: the thin-arcs approximation

Arnaud Cassan^{*}

Institut d'Astrophysique de Paris, Sorbonne Université, CNRS, UMR 7095, 98 bis bd Arago, F-75014 Paris, France

Received / Accepted

ABSTRACT

Long baseline interferometry of microlensing events can resolve the individual images of the source produced by the lens, which combined with the modelling of the microlensing light curve, leads to the exact lens mass and distance. Interferometric observations thus offer a unique opportunity to constrain the mass of exoplanets detected by microlensing, and to precisely measure the mass of distant isolated objects such as stars and brown dwarfs, and of stellar remnants such as white dwarfs, neutron stars, and stellar black holes. Having accurate models and reliable numerical methods is of particular importance as the number of targets is expected to increase significantly in the near future. In this work we discuss the different approaches to calculating the fringe complex visibility for the important case of a single lens. We propose a robust integration scheme to calculate the exact visibility, and introduce a novel approximation, which we call the 'thin-arcs approximation', which can be applied over a wide range of lens–source separations. We find that this approximation runs six to ten times faster than the exact calculation, depending of the characteristics of the event and the required accuracy. This approximation provides accurate results for microlensing events of medium to high magnification observed around the peak (i.e. a large fraction of potential observational targets).

Key words. Gravitational lensing: micro, Techniques: interferometric, Methods: numerical

1. Introduction

Measuring the mass of isolated objects in our Milky Way is a major challenge in astrophysics, whether it be the mass of stars, brown dwarfs, or stellar remnants such as white dwarfs, neutron stars, or stellar black holes. Few observational techniques allow such measurements to be made with high precision and/or independently of assumptions about the structure of the targeted objects. Gravitational microlensing (Paczynski 1986), based on the deflection of light rays by a lensing body transiting the line of sight of a distant star, provides the solution of choice for measuring the mass of such isolated lenses. The technique allows us to probe objects, intrinsically luminous or not, up to Galactic scales and independently of the light emitted by the lens itself.

Microlensing affects the shape and the number of images of the source star, which results in a global enhancement of the total flux received by the observer. As the individual images produced by the microlens cannot be separated by classical telescopes, what is usually measured is the increase (or magnification) in the flux of the source star as a function of time. Nevertheless, when for bright-enough microlensing events, the lensed images can in principle be resolved with long baseline interferometers (Delplancke et al. 2001; Dalal & Lane 2003; Rattenbury & Mao 2006; Cassan & Ranc 2016) since their typical separation is of the order of a milliarcsecond (i.e. within the reach of interferometers with baselines of ~ 40 – 100 metres. A first series of successful interferometric observations was recently made with the Very Large Telescope Interferometer (ESO/VLTI) on microlensing events TCP J05074264+2447555 'Kojima-1' (Dong et al. 2019) and Gaia19bld (Cassan et al. 2022).

To measure the mass of the lens, two quantities must be derived from the observations. The first is π_E , the microlensing parallax; the second is θ_E , the angular Einstein ring radius, which is the angular radius of the ring-like image of the source were it to be perfectly aligned with the lens. The mass follows from $M = \theta_E / \kappa \pi_E$, where $\kappa = 8.144 \text{ mas}/M_\odot$ (Gould 2000). Ground-based observations can access π_E for long-lasting microlensing events, for which the transverse motion of the Earth is significant enough to allow a good parallax measurement, while for shorter microlensing events space-based parallax is in general required to provide a different vantage point from Earth. Classically, θ_E can be estimated from the photometric light curve if the spatial extension of source reveals itself by producing noticeable deviations in the light curve and if the source star is well characterised; in the case of bright microlenses, high-resolution adaptive-optics imaging can also access θ_E typically 5–10 years after the microlensing event is over, when the background star and the microlens can be resolved individually. As for long baseline interferometry, it provides a direct measurement of θ_E by resolving the split images of the source star and measuring their angular separations. An additional constraint on π_E can be obtained when times series observations are performed as they allow the direction of the relative motion between the lens and the source to be measured (Cassan et al. 2022).

The modelling of interferometric data requires both robust and efficient numerical methods to compute the microlensing models, with a good control on numerical errors, in order to calculate the wide range of models typically required by Markov chain Monte Carlo (MCMC) algorithms. In this work we discuss in detail the case of single-lens models. In Section 2 we propose a new and more efficient approach for the exact calculation of the complex interferometric visibility than exists in the

^{*} arnaud.cassan@iap.fr

literature; we also establish a new approximation, called the thin-arcs approximation, which runs six to ten times faster than the exact calculation, and should apply to a large fraction of potential observational targets. In Section 3 we illustrate and discuss the domain of validity of the thin-arcs approximation by comparing it to the exact calculation, and also to the point-source approximation. We discuss the possible shortcomings of ill-defined parametrisations, and advocate for suitable sets of parameters that depend on the characteristics of the observed microlensing event. Finally, in Section 4 we summarise the main results and discuss the perspectives of optical/infrared long baseline interferometric observations of microlensing events, in particular in the context of recent developments of the ESO VLTI/GRAVITY instrument.

2. Visibility of reference single-lens models

2.1. Key concepts and equations

The lens equation relates the angular position of the background source star to that of its multiple images. If we set up a Cartesian frame of reference (O, x, y) with axes fixed in the plane of the sky (e.g. north, east) and if we choose the lens to be at the centre of the coordinate system, the complex lens equation for an isolated massive body reads

$$\zeta = z - \frac{1}{\bar{z}}, \quad (1)$$

where ζ is the affix of the (point-like) centre of the source, z the affix of one of the individual point-like images, and \bar{z} the complex conjugate of z . For the lens equation to be correct, the quantities ζ and z are further normalised by θ_E , the Einstein angular ring radius (Einstein 1936), which is a function of the lens mass M , the observer-lens distance D_L , and the observer-source distance D_S through

$$\theta_E \equiv \sqrt{\frac{4GM}{c^2} \left(\frac{D_S - D_L}{D_S D_L} \right)}, \quad (2)$$

with c is the speed of light and G the gravitational constant. The typical separation of the images is of the order of θ_E ; when the source, lens, and observer are perfectly aligned, the image is seen as a perfect ring-shaped image, called an Einstein ring. For a given position $\zeta = u_1 e^{i\theta}$ of the source centre \mathcal{S} (Figure 1), the single lens equation Eq. (1) is easily solved by writing $z = r e^{i\theta}$, with r solution of $r^2 - u_1 r - 1 = 0$. This yields two solutions for the images, $z^{(\pm)} = r^{(\pm)} e^{i\theta}$, where

$$r^{(\pm)} = \frac{u_1 \pm \sqrt{u_1^2 + 4}}{2}. \quad (3)$$

If we assume $u_1 > 0$, the image with $r^{(+)} > 0$ is the major image ($\mathcal{I}^{(+)}$ in Figure 1) and that with $r^{(-)} < 0$ is the minor image ($\mathcal{I}^{(-)}$ in the figure). As ζ , $z^{(+)}$, and $z^{(-)}$ have the same argument, \mathcal{S} , $\mathcal{I}^{(+)}$, and $\mathcal{I}^{(-)}$ are aligned together with the lens, as shown in Figure 1. If the lens is perfectly aligned with the lens (i.e. $\zeta = 0$), then Eq. (1) yields $|\zeta| = 1$ and the image is an Einstein ring of physical angular radius θ_E . To avoid any confusion in the units in the angular quantities we discuss here, in the following we assign a subscript ‘E’ to all angular coordinates expressed in θ_E units. Hence, we write $\zeta \equiv \xi_E + i\eta_E$ and $z \equiv x_E + iy_E$, with

$$(x_E, y_E) \equiv (x, y) / \theta_E, \quad (4)$$

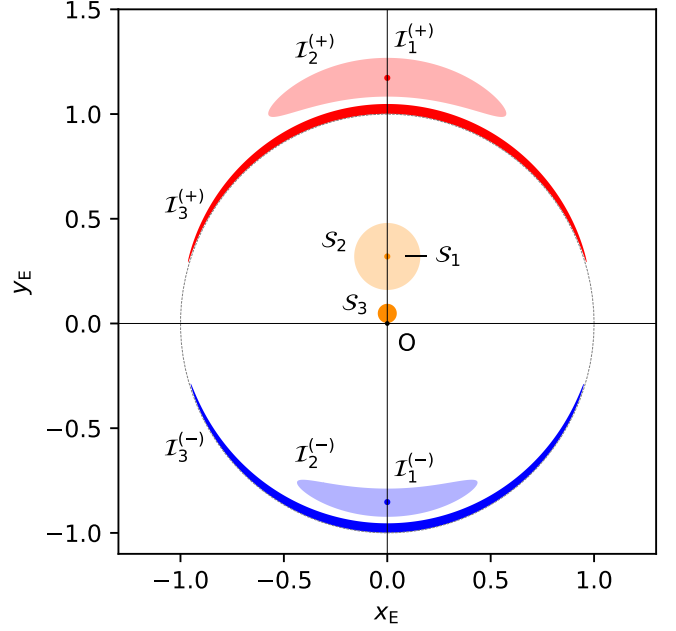


Fig. 1. Schematics of the three reference single-lens models detailed in the text. In all cases, the source centre lies on the y_E -axis, and the source surface is uniformly bright. Both axes are in θ_E units. The microlens is the black dot at the centre of the frame, and the Einstein ring is indicated by the dotted circle of radius unity. In the point-source approximation, the source star \mathcal{S}_1 (in orange) is point-like and has two point-like images: the major image $\mathcal{I}_1^{(+)}$ (in red) is located outside of the Einstein ring, while the minor image $\mathcal{I}_1^{(-)}$ (in blue) is inside. In general, a source \mathcal{S}_2 has a spatial extension, and its major and minor images $\mathcal{I}_2^{(+)}$ and $\mathcal{I}_2^{(-)}$ are elongated along the Einstein ring. When both the source radius and the lens-source separation are smaller than unity, as for source \mathcal{S}_3 , the two images take the form of two thin arcs, $\mathcal{I}_3^{(+)}$ and $\mathcal{I}_3^{(-)}$. When the microlens lies inside the source, the two images merge into a single ring-like image (not shown here).

where (x, y) are expressed in radians and (x_E, y_E) in θ_E units.

The complex (fringe) visibility measured by the interferometer is the Fourier transform of the spatial distribution of light $I(x_E, y_E)$ in the plane of the sky (more precisely here, the surface brightness of the images), or

$$\mathcal{F}[I](u_E, v_E) \equiv \iint_{\mathbb{R}^2} I(x_E, y_E) e^{-i2\pi(u_E x_E + v_E y_E)} dx_E dy_E, \quad (5)$$

where (u_E, v_E) are the conjugate coordinates of (x_E, y_E) . The latter are thus expressed as

$$(u_E, v_E) \equiv (u, v) \times \theta_E, \quad (6)$$

where (u, v) are the usual spatial frequencies, related to the projected baselines B_u and B_v (respectively in the (Ox) and (Oy) directions) by $u = B_u/\lambda$ and $v = B_v/\lambda$, with λ the wavelength of observations; (u, v) are expressed in radians and (u_E, v_E) in θ_E^{-1} units (Cassan & Ranc 2016). Hereafter, we also call ‘visibility’ the quantity

$$V_E(u_E, v_E) \equiv \frac{\mathcal{F}[I](u_E, v_E)}{\mathcal{F}[I](0, 0)}, \quad (7)$$

which is a normalised version of Eq. (5), as the term in the denominator is the total flux. The squared visibility is the squared modulus of the visibility, $|V_E|^2$, and its phase is $\phi = \arg V_E$.

We now consider a circular uniformly bright source of constant surface brightness $I(x_E, y_E) = I_S$, lensed by an isolated massive body (limb-darkened sources are treated in Section 2.5). As I_S cancels out in the expression of V_E in Eq. (7), it is convenient to use the quantity $\Phi \equiv \mathcal{F}[I]/I_S$ (which we also call ‘visibility’ for simplicity); for the lensed images, we then have

$$\Phi_{\mu l}(u_E, v_E) = \iint_{\mathcal{I}} e^{-i2\pi(u_E x_E + v_E y_E)} dx_E dy_E, \quad (8)$$

where the subscript ‘ μl ’ stands for microlensed. The integration is performed within the boundaries \mathcal{I} of the (multiple) lensed images. These images are elongated around the Einstein ring, as shown in Figure 1 for the \mathcal{S}_2 and \mathcal{S}_3 sources.

In addition to the lensed images of the source, bright stars in the observing line of sight, although not magnified by the lens, may also be considered as contributing ‘blend’ stars of total visibility Φ_B . In particular, if the lens itself is bright enough, it may indeed contribute to a blend term Φ_L . Other stars than the lens are unlikely to be involved, even in crowded fields in the Galactic bulge region, because most stars in the immediate vicinity of the lens are faint. We define the blending factor of individual blend star k as the ratio

$$g_k \equiv F_{B_k}/F_S, \quad (9)$$

where F_{B_k} is the flux of blend star k and $F_S = I_S S$ the flux of the source when it is not lensed, with $S = \pi\rho^2$ and ρ the radius of the source in θ_E units. We justify that I_S is used to calculate the flux of both the source and its lensed images, as gravitational lensing has the important property of preserving surface brightness when forming the lensed images. For a given blend star k of surface S_k (in θ_E^2 units), the star’s (constant) surface brightness reads $I_{B_k} \equiv F_{B_k}/S_k = g_k S I_S/S_k$. As in general these stars are not resolved by the interferometer (including the lens; a typical solar-mass lens at 4 kpc has an angular diameter of about $2 \mu\text{as}$), S_k can be considered infinitely small and we can write $I_{B_k} = g_k S I_S \delta(x_E - x_{E_k}) \delta(y_E - y_{E_k})$, with δ the Dirac distribution and (x_{E_k}, y_{E_k}) the coordinates of star k . Considering all blend stars, the surface brightness reads

$$I_B(x_E, y_E) = \sum_k I_{B_k} = I_S \pi\rho^2 \sum_k g_k \delta(x_E - x_{E_k}) \delta(y_E - y_{E_k}), \quad (10)$$

so that the blend visibility is given by

$$\Phi_B(u_E, v_E) = \pi\rho^2 \sum_k g_k e^{-i2\pi(u_E x_{E_k} + v_E y_{E_k})}. \quad (11)$$

In particular, a bright lens (in the centre of the frame) would contribute to $\Phi_L = g_L \pi\rho^2$, with $g_L = F_L/F_S$ the blend-to-source flux ratio. The overall visibility is expressed as

$$V_E(u_E, v_E) = \frac{\Phi_{\mu l} + \Phi_B}{\Phi_{\mu l_0} + \Phi_{B_0}}, \quad (12)$$

where $\Phi_{\mu l_0} \equiv \Phi_{\mu l}(0, 0)$ and $\Phi_{B_0} \equiv \Phi_B(0, 0)$. When three or more baselines are involved, the bispectrum $B_{E,1,2,3}$ and closure phase $\phi_{E,T3}$ of each triangle of baselines are given by

$$B_{E,1,2,3} = V_E(u_{E,1}, v_{E,1}) \times V_E(u_{E,2}, v_{E,2}) \times V_E(u_{E,3}, v_{E,3}), \quad (13)$$

$$\phi_{E,T3} = \arg(B_{E,1,2,3}), \quad (14)$$

where $(u_{E,3}, v_{E,3}) = -(u_{E,1}, v_{E,1}) - (u_{E,2}, v_{E,2})$ (or an equivalent formula considering that $V_E(-u_E, -v_E) = \overline{V_E(u_E, v_E)}$).

For an interferometer observing in the H band ($\lambda \approx 1.65 \mu\text{m}$) with projected baseline $B = 100$ m along the x -axis, and typical

values of θ_E of 0.5, 1, 1.5, and 2 mas, the interferometer probes u_E -values of 0.15, 0.30, 0.45, and 0.60 (in θ_E^{-1} units). As the angular separation of the major and minor images is $\sim 2 \times \theta_E$ (see Figure 1), we expect the visibility to be modulated with a period of ~ 0.5 along u_E , with a first minimum at $u_E \sim 0.25$ (in θ_E^{-1} units). This means that provided the microlensing event is bright enough to be observed, the lensed images can be resolved in most cases, and the value of θ_E measured.

In the following sections, we derive suitable formulae to compute efficiently Eq. (8) for three reference single-lens models: the point-source approximation, the exact formula, and a novel thin-arcs approximation, for uniform and limb-darkened sources.

2.2. Point-source approximation

The visibility for a single lens in the point-source approximation was first studied by Delplancke et al. (2001). The resulting major and minor point-like images can then be modelled by Dirac distributions, respectively located at $r^{(+)}$ and $r^{(-)}$, from Eq. (3) and Figure 1, and weighted by their individual magnification factor $\mu^{(+)}$ and $\mu^{(-)}$ given by

$$\mu^{(\pm)} = \frac{1}{2} \left| 1 \pm \frac{u_1^2 + 2}{u_1 \sqrt{u_1^2 + 4}} \right|. \quad (15)$$

When there is no source of blend (Delplancke et al. 2001), the squared visibility reads

$$\begin{aligned} |V_E|^2 &= \left| \frac{\mu^{(+)} e^{-i2\pi v_E r^{(+)}} + \mu^{(-)} e^{-i2\pi v_E r^{(-)}}}{\mu^{(+)} + \mu^{(-)}} \right|^2 \\ &= \frac{1 + R^2 + 2R \cos\left(2\pi v_E \sqrt{u_1^2 + 4}\right)}{(1 + R^2)^2}, \end{aligned} \quad (16)$$

where $R = \mu^{(+)}/\mu^{(-)}$ is the ratio of the magnification of the major image to that of the minor image. The quantity $|V_E|^2$ is a sinusoidal function along the (Oy_E) direction, and is invariant along the (Ox_E) direction. The modulation has a period of $T = 1/(u_1^2 + 4)^{1/2}$ and the squared visibility oscillates between $\left(\frac{R-1}{R+1}\right)^2$ and 1. If u_1 is not too large (i.e. $u_1 \lesssim 0.5$), the periodicity is approximately constant and equal to $T \approx 0.5$. The amplitude is largest when u_1 is small, as $\mu^{(+)}$ and $\mu^{(-)}$ are both approximated by $1/2u_1$ so that $R \approx 1$. However, we show in Section 3 that the point-source model provides in this case a poor approximation of the visibility as the lens strongly distorts the images.

In the general case when one or several unrelated objects k contribute to the blending flux (Sect. 2.1), the resulting complex visibility reads

$$V_E = \frac{\mu^{(+)} e^{-i2\pi v_E r^{(+)}} + \mu^{(-)} e^{-i2\pi v_E r^{(-)}} + \sum_k g_k e^{-i2\pi(u_E x_{E_k} + v_E y_{E_k})}}{\mu^{(+)} + \mu^{(-)} + \sum_k g_k}, \quad (17)$$

where (x_{E_k}, y_{E_k}) are the location of the blend sources on the plane on the sky in θ_E units, and g_k their blending factors as defined by Eq. (9).

Finally, we note that a single lens event will always lead to a strong interferometric signal, even for microlensing events with relatively low peak magnification or observed far from the peak of the light curve. From the definition of R in Eq. (16) and Eq. (15), it is possible to compute the maximum amplitude of the oscillation of V_E^2 , which is equal to $S = 1 - \left(\frac{R-1}{R+1}\right)^2 = 4/(u_1^2 + 2)^2$.

Even for an unrealistic observation at very low magnification (e.g. 1.4; $u_1 = 0.9$), we have $S > 0.5$, and for a more standard value of $u_1 < 0.2$ (magnification > 5), the contrast reaches values greater than $S > 0.96$.

2.3. Exact formula for an extended source star

The visibility and closure phase for an extended-source single-lens model was first studied by Rattenbury & Mao (2006). As the images are elongated along the Einstein ring (Figure 1) with analytically well-defined contours (Section 2.1), the authors proposed computing numerically the visibility defined in Eq. (5) by a line integral along the outer boundary of each of the major and minor images.

Here, however, we follow a different route and set up another approach to compute Eq. (5), motivated by different arguments. Firstly, our tests have shown that while the line integration scheme works well when the images are reasonably elongated (i.e. at low to medium magnifications), when the images take the form of thin arcs the parametrisation of the contours is far from optimal, as the individual points defining the images contours become strongly unevenly spaced. To achieve reasonable accuracy, the points on the contours need to be resampled, and in any case the number of contour points must be significantly increased. This operation is mandatory, as the line integral basically operates a subtraction between the wedge-shaped area subtended by the outer boundary and that subtended by the inner boundary, which are both of the order of $\varphi/2$ (as they are located at $r \simeq 1$), where φ is the opening angle defined in Figure 2. In contrast, when $\rho \ll 1$ the area enclosed in a given image is of the order of $\rho\varphi$, and the fractional difference corresponding to the searched visibility is of the order of $\rho\varphi/(\varphi/2) = 2\rho \ll 1$. Hence, an accurate visibility requires a very high accuracy on the line integrals, in particular in the portions where the contours are not well sampled by the parametrisation. The approach we derive below is both robust and computationally much more efficient, and allows a precise control on the final accuracy. This can be achieved by calculating Eq. (5) as a two-dimensional integral in polar coordinates, as we detail below.

We again let $u_1 > 0$ be the ordinate of the centre of the source S along the y_E -axis, and ρ the source radius (both in θ_E units), as shown in Figure 3. We again assume that the source is uniformly bright (and also the images, since surface brightness is preserved). We let θ be the angle of the usual polar coordinates, and u_+ and u_- the radii where the radial black line in Figure 3 intersects the upper and lower contours of the source. From geometrical considerations, these are given by

$$u_{\pm} = u_1 \cos \beta \pm \sqrt{\rho^2 - u_1^2 \sin^2 \beta}, \quad (18)$$

where $\beta \equiv \theta - \pi/2$. If $\rho < u_1$, we restrict β to vary between $-\arcsin \eta_1$ and $\arcsin \eta_1$ (left panel of Figure 3), where

$$\eta_1 \equiv \rho/u_1. \quad (19)$$

Otherwise, if $0 < u_1 < \rho$, we limit β to vary between $-\pi/2$ and $\pi/2$ (right panel). These choices are sufficient to parametrise the two arc-shaped images (or the ring) as we obtain two points above the horizontal axis for the major image $\mathcal{I}^{(+)}$, $r_+^{(+)}$, and $r_-^{(+)}$, and two points below for the minor image $\mathcal{I}^{(-)}$, $r_+^{(-)}$, and $r_-^{(-)}$,

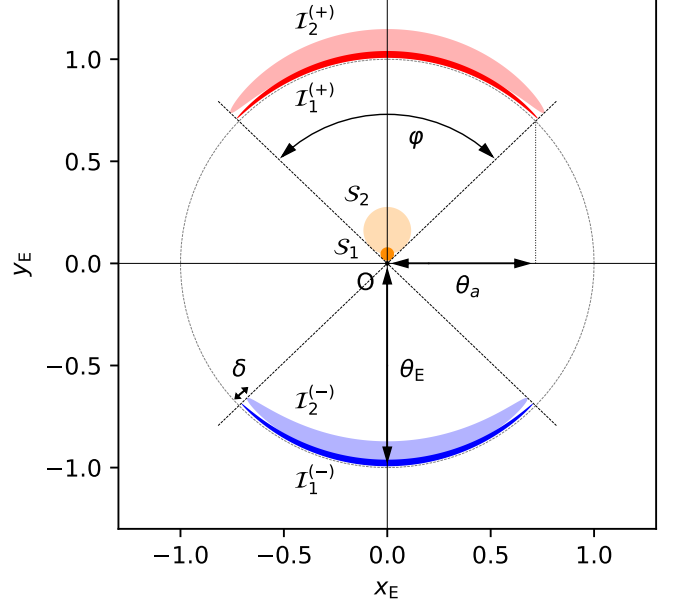


Fig. 2. Geometry of major (red) and minor (blue) images when the images are arc-shaped (i.e. for $0 < \eta_1 < 1$, where $\eta_1 = \rho/u_1$). The Einstein ring is shown as the black dotted circle, and both axes are in θ_E units. When the arcs are thin, the images thickness δ is not resolved by the interferometer and two sources S_1 and S_2 (in orange) of same ratio η_1 produce arc-shaped images of equal angular elongation, $\varphi = 2 \arcsin \eta_1$. The projected extension of the arcs onto the x_E -axis is $\theta_a = \eta_1 \theta_E$, is hence comparable to θ_E , and is thus resolved by the interferometer. When $\eta_1 > 1$, the image of the source is a ring (and $\varphi = \pi$).

given by

$$\begin{cases} r_{\pm}^{(+)} = \frac{1}{2} \left(u_{\pm} + \sqrt{u_{\pm}^2 + 4} \right) \\ r_{\pm}^{(-)} = \frac{1}{2} \left(u_{\pm} - \sqrt{u_{\pm}^2 + 4} \right) \end{cases} \quad (20)$$

from Eq. (3). In all cases, $r_-^{(-)} < r_+^{(-)} < 0 < r_-^{(+)} < r_+^{(+)}$. If $u_1 = 0$, the ring is perfectly symmetric (Einstein ring) as $u_{\pm} = \pm\rho$, so that $r_-^{(-)} = -r_+^{(+)}$ and $r_+^{(-)} = -r_-^{(+)}$. To calculate the visibility, we further perform the integration of Eq. (8) in polar coordinates,

$$\begin{aligned} \Phi_{\mu l} &= \iint_I e^{-i2\pi r(u_E \cos \theta + v_E \sin \theta)} r dr d\theta \\ &= \iint_I e^{-i2\pi \Omega r} r dr d\theta, \end{aligned} \quad (21)$$

where

$$\Omega \equiv u_E \cos \theta + v_E \sin \theta. \quad (22)$$

We also decompose the full integral into two separate integrals, one for the image above the horizontal axis (elongated image or half-ring), $\Phi^{(+)}$, and one for the image below, $\Phi^{(-)}$, with

$$\Phi_{\mu l} = \Phi^{(+)} + \Phi^{(-)}. \quad (23)$$

We first consider the case $\rho < u_1$ (or $0 < \eta_1 < 1$). Since $0 < r_-^{(+)} < r_+^{(+)}$ and $\pi/2 - \arcsin \eta_1 \leq \theta \leq \pi/2 + \arcsin \eta_1$, we can

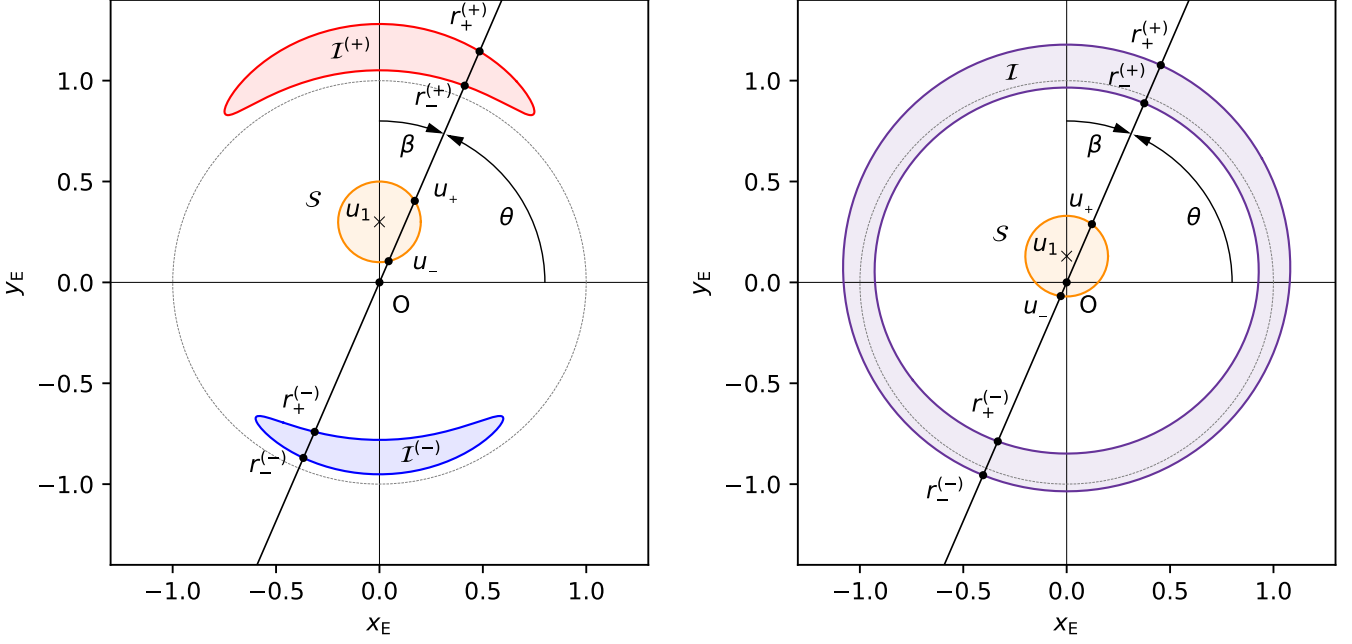


Fig. 3. Geometry and parameters used to calculate interferometric visibility of an extended source star lensed by a single lens. In both panels the Einstein ring is shown as the black dotted circle, and both axes are in θ_E units. $u_1 \geq 0$ is the position of the centre of the source along the y_E -axis, u_+ and u_- are the intersections of the black line (polar angle θ) with the contour of the source, and $(r_+^{(+)}, r_+^{(-)})$ and $(r_-^{(+)}, r_-^{(-)})$ are their respective images given by the single-lens equation. Arc-like images are shown in the left panel ($0 < \eta_1 < 1$, where $\eta_1 = \rho/u_1$), while the case of a single ring-like image ($\eta_1 > 1$) is shown on the right.

write the integral Eq. (21) for the major image as

$$\begin{aligned} \Phi^{(+)} &= \int_{\pi/2 - \arcsin \eta_1}^{\pi/2 + \arcsin \eta_1} \left(\int_{r_-^{(+)}}^{r_+^{(+)}} r e^{-i2\pi\Omega r} dr \right) d\theta \\ &= \int_{-\arcsin \eta_1}^{\arcsin \eta_1} R(r_-^{(+)}, r_+^{(+)}) d\beta, \end{aligned} \quad (24)$$

where we change to variable β in the second line,

$$\Omega = -u_E \sin \beta + v_E \cos \beta, \quad (25)$$

and

$$\begin{aligned} R(r_1, r_2) &\equiv \int_{r_1}^{r_2} r e^{-i2\pi\Omega r} dr \\ &= \begin{cases} \frac{1}{2} (r_2^2 - r_1^2) & \text{if } \Omega = 0, \\ \left[\frac{e^{-i2\pi\Omega r} (1 + i2\pi\Omega r)}{4\pi^2\Omega^2} \right]_{r_1}^{r_2} & \text{otherwise.} \end{cases} \end{aligned} \quad (26)$$

The first terms of the series expansion (with respect to Ω) of the expression inside the brackets are

$$\frac{e^{-i2\pi\Omega r} (1 + i2\pi\Omega r)}{4\pi^2\Omega^2} \approx \frac{r^2}{2} + \frac{1}{4\pi^2\Omega^2} - \frac{2}{3}\pi r^3\Omega - \frac{1}{2}\pi^2 r^4\Omega^2. \quad (27)$$

When $\Omega \ll 1$, the term $1/4\pi^2\Omega^2$ becomes large, possibly generating numerical issues, although theoretically this term cancels out in the difference Eq. (26). Hence, the formula $(r_2^2 - r_1^2)/2$ may be used for values of Ω below a threshold of typically $\Omega \sim 10^{-3}$ if we want the second term of the series (in Δr^3) to contribute no more than $\sim 10^{-3}$ times the term in Δr^2 .

We proceed in a similar way for the minor image, but this time with $r_-^{(-)} < r_+^{(-)} < 0$ and $-\pi/2 - \arcsin \eta_1 \leq \theta \leq -\pi/2 + \arcsin \eta_1$, so that the integral reads

$$\begin{aligned} \Phi^{(-)} &= \int_{-\pi/2 - \arcsin \eta_1}^{-\pi/2 + \arcsin \eta_1} \left(\int_{-r_+^{(-)}}^{-r_-^{(-)}} r e^{-i2\pi\Omega r} dr \right) d\theta \\ &= \int_{-\arcsin \eta_1}^{\arcsin \eta_1} \left(\int_{-r_+^{(-)}}^{-r_-^{(-)}} r e^{i2\pi\Omega' r} dr \right) d\beta', \end{aligned} \quad (28)$$

after changing the variable to $\beta' = \theta + \pi/2$, and introducing $\Omega' = -u_E \sin \beta' + v_E \cos \beta' = -[u_E \cos(\beta' - \pi/2) + v_E \sin(\beta' - \pi/2)] = -\Omega$. As β' is a dummy variable, we call it β and write

$$\begin{aligned} \Phi^{(-)} &= \int_{-\arcsin \eta_1}^{\arcsin \eta_1} \left(\int_{-r_+^{(-)}}^{-r_-^{(-)}} r e^{i2\pi\Omega r} dr \right) d\beta \\ &= \int_{-\arcsin \eta_1}^{\arcsin \eta_1} \left(\int_{r_+^{(-)}}^{r_-^{(-)}} r e^{-i2\pi\Omega r} dr \right) d\beta \\ &= \int_{-\arcsin \eta_1}^{\arcsin \eta_1} \left(- \int_{r_+^{(-)}}^{r_-^{(-)}} r e^{-i2\pi\Omega r} dr \right) d\beta \end{aligned} \quad (29)$$

by changing variable r to $-r$ and inverting the boundaries of the integral, so that

$$\Phi^{(-)} = \int_{-\arcsin \eta_1}^{\arcsin \eta_1} -R(r_-^{(-)}, r_+^{(-)}) d\beta. \quad (30)$$

We now examine the case $0 < u_1 < \rho$ (or $\eta_1 > 1$). In this situation the lens lies inside the source, and there is a single ring-like image. The full ring can be drawn by varying θ from 0 to π , as $r_+^{(+)}$ and $r_-^{(+)}$ draw the half-ring above the horizontal axis and $r_+^{(-)}$ and $r_-^{(-)}$ the half ring below it. Hence, the calculation is

exactly the same as for $\rho < u_1$; the only difference is that the integration is now performed between $-\pi/2 \leq \beta \leq \pi/2$.

In summary, for all values of $u_1 > 0$ and $\rho > 0$ (i.e. $\eta_1 > 0$) we have

$$\Phi_{\mu l} = \int_{-\beta_m}^{\beta_m} \left[R(r_-^{(+)}, r_+^{(+)}) - R(r_-^{(-)}, r_+^{(-)}) \right] d\beta, \quad (31)$$

where

$$\beta_m \equiv \arcsin[\min(\eta_1, 1)]. \quad (32)$$

When $u_1 = 0$ (Einstein ring), this formula still holds with $\beta_m = \pi/2$. In that case the visibility has no imaginary part, which is expected from the symmetry of the ring image.

2.4. The thin-arcs approximation

We consider a common case in practice where the source has a small radius ρ compared to θ_E (typically, $\rho \lesssim 0.1$) and passes the lens at small impact parameter, typically $u_1 \lesssim 0.2$ (which corresponds to a point-source magnification at a peak of about 5). This situation is illustrated in Figure 2 for two sources of radii \mathcal{S}_1 and \mathcal{S}_2 . In the figure it is clear that if the major and minor images are resolved by the interferometer along the (Oy_E) axis (typical angular separation of $2 \times \theta_E$, cf. Figure 2), they have a good chance to be resolved along the (Ox_E) axis as well (typical angular separation of $2 \times \theta_a$, where ‘ a ’ stands for arcs). Since the opening angle of the images is given by $\varphi = 2 \arcsin \eta_1$ (with $\eta_1 = \rho/u_1 < 1$, and $\varphi = \pi$ for a ring-like image), we have $\theta_a = \eta_1 \theta_E$ (or $\theta_a = \theta_E$ for a ring). Values of $\eta_1 > 0.5$ are easily reached for the range of values of u_1 we discussed above. Hence, we expect this situation to be common in observed microlensing events.

While the major and minor images are resolved in their individual elongations ($\sim 2\theta_a$) and mutual separation ($\sim 2\theta_E$), on the contrary their thickness (δ in Figure 2) will most certainly never be resolved by current interferometric facilities: a value of δ of the order of ρ requires reaching, at best, typical angular resolutions of $\delta \approx \rho \theta_E < 10 \mu\text{as}$. Measuring the thickness of the arcs, however, is not in itself a requirement for measuring θ_E , as the thickness and the extension of the arcs are directly related by the model. It simply means that the source size ρ is not measured directly by interferometry, but it does not matter in practice as ρ is usually obtained from the modelling of the photometric light curve. It thus appears natural to investigate the possibility of an approximation formula for the visibility that does not directly depend on ρ . A second argument for it is that, as shown in Figure 2, two sources of different radii but with same opening angle φ (i.e. the same value of η_1) are difficult to distinguish from an interferometric point of view, as the displacement is again of the order of $\rho \theta_E$. Hence, a natural model parameter for the sought-after approximation is η_1 (i.e. the ratio of ρ/u_1 instead of the parameters ρ and u_1 individually). Conversely, if ρ to u_1 are used in the situation of arc-shaped images (using the exact formula given in Section 2.3), we expect these parameters to be strongly correlated (if not degenerate), which may alter the smooth running of the fitting process when modelling interferometric data.

To further illustrate this aspect, Figure 4 shows the difference in squared visibility $\Delta|V_E|^2$ between a model computed for parameters $\rho = 0.05$ and $u_1 = 8.3 \times 10^{-2}$, and a reference model obtained with $\rho = 0.001$ and $u_1 = 1.7 \times 10^{-3}$, so that both models have same parameter $\eta_1 = 0.6$. It appears from the figure that while the source radius is multiplied by a factor of 50 between

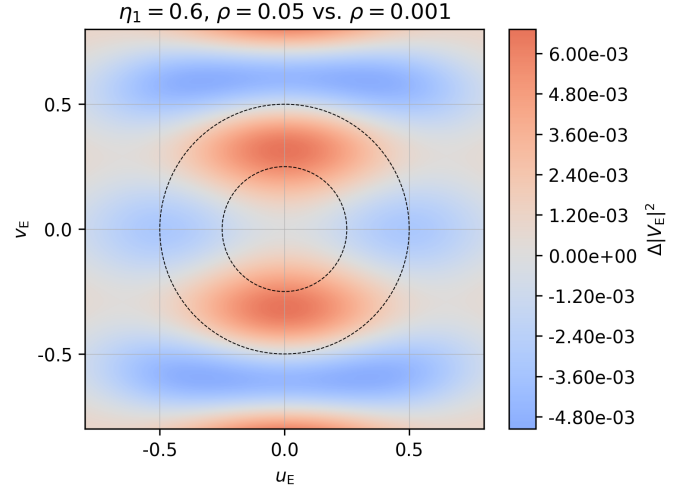


Fig. 4. Difference in squared visibility between two single-lens models with same parameter $\eta_1 = 0.6$. Both axes are in θ_E^{-1} units. The inner dashed circle indicates the typical angular resolution (radius 0.25) and the outer circle (radius 0.5) twice the typical resolution. The reference model has a source radius $\rho = 10^{-3}$ (with $u_1 = 1.7 \times 10^{-3}$), while the second model has a source 50 times larger, $\rho = 5 \times 10^{-2}$ (with $u_1 = 8.3 \times 10^{-2}$). In this case the maximum difference in squared visibility is about 6×10^{-3} , in practice well below the noise. It justifies the use of η_1 in the modelling instead of parameters ρ and u_1 .

the two models, the squared visibility is not changed by more than 6×10^{-3} (for a maximum excursion between 0 and 1).

To establish a suitable approximation, which we call the thin-arcs approximation, we note that when both ρ and u_1 are small (see Section 3.1), u_{\pm} are small as well so that we can expand $r_{\pm}^{(\pm)}$ to first order in u_{\pm} :

$$\begin{cases} r_{\pm}^{(+)} \approx 1 + \frac{u_{\pm}}{2} \\ r_{\pm}^{(-)} \approx -1 + \frac{u_{\pm}}{2} \end{cases}. \quad (33)$$

Calculating R in Eq. (26) for $\Omega \geq 0$ yields

$$\begin{cases} R(r_-^{(+)}, r_+^{(+)}) = e^{-i2\pi\Omega} \sqrt{\rho^2 - u_1^2 \sin^2 \beta} \\ R(r_-^{(-)}, r_+^{(-)}) = -e^{i2\pi\Omega} \sqrt{\rho^2 - u_1^2 \sin^2 \beta}, \end{cases} \quad (34)$$

which allows us to write, in Eq. (31),

$$R(r_-^{(+)}, r_+^{(+)}) - R(r_-^{(-)}, r_+^{(-)}) = 2 \cos(2\pi\Omega) \sqrt{\rho^2 - u_1^2 \sin^2 \beta}. \quad (35)$$

From Eq. (25), the real part of $\cos(2\pi\Omega)$ is the product $\cos(2\pi u_E \sin \beta) \times \cos(2\pi v_E \cos \beta)$, while its imaginary part reads $-\sin(2\pi u_E \sin \beta) \times \sin(2\pi v_E \cos \beta)$. As we integrate from $-\beta_m$ to β_m , the imaginary part cancels out while the real part is doubled. Finally, for $u_1 > 0$ the visibility reads¹

$$\Phi_{\mu l} = 4u_1 \int_0^{\beta_m} f(\beta) d\beta, \quad (36)$$

¹ The denominator of V_E in Eq. (12), $\Phi_{\mu l_0} = \Phi_{\mu l}(0,0)$, can be written as $\Phi_{\mu l_0} = 4\rho E(\beta_m, \eta_1^{-2})$, where $E(\phi, m) = \int_0^{\phi} (1 - m \sin^2 \theta)^{1/2} d\theta$ is the incomplete elliptic integral of the second kind. The total source flux magnification A being the ratio of the total area of the images $\Phi_{\mu l_0}$ to the area of the source, $\pi\rho^2$, we obtain $A = (4/\pi\rho)E(\beta_m, \eta_1^{-2})$, which is the approximation derived by Yoo et al. (2004), though with a slightly different definition of E and $z = 1/\eta_1$.

where again $\beta_m = \arcsin[\min(\eta_1, 1)]$ and

$$f(\beta) = \cos(2\pi u_E \sin \beta) \cos(2\pi v_E \cos \beta) \sqrt{\eta_1^2 - \sin^2 \beta}, \quad (37)$$

while for $u_1 = 0$ (Einstein ring),

$$\Phi_{\mu l} = 4\rho \int_0^{\frac{\pi}{2}} \cos(2\pi u_E \sin \beta) \cos(2\pi v_E \cos \beta) d\beta. \quad (38)$$

As expected, the integrand Eq. (37) does not depend on ρ and u_1 individually, but on their ratio η_1 (for the perfect Einstein ring, the integrand Eq. (38) does not depend of any of these parameters). In both cases (assuming no blend stars, or $\Phi_B = 0$), the factors $4u_1$ or 4ρ cancel out in Eq. (12), so that the visibility V_E depends on η_1 only for $u_1 > 0$. It is noteworthy that in the thin-arcs approximation, $\phi = \arg \Phi_{\mu l}$ can take only two values, 0 and π . It means that the bispectrum $B_{E,1,2,3}$ in Eq. (13) is also real, and the closure phases $\phi_{E,T3}$ in Eq. (14) are 0 or π . As u_1 increases, the exact value of $\phi_{E,T3}$ starts to differ from these two values, and should be calculated with the exact formula derived in Section 2.3.

Our numerical simulations show that the thin-arcs approximation speeds up the computation by a factor of 6 to 10 (depending on the specific configuration of the images) compared to the exact formula, under a common implementation in Python using the `scipy/romberg` integration scheme and a given achieved accuracy (5×10^{-5}) on both the real and imaginary parts of V_E . As we further discuss in Section 3.1, the domain of validity of the thin-arcs approximation is wide. Considering $|V_E|^2$, for the usual values of ρ and typical excursions in the $u_E v_E$ -plane, the point-source approximation can be linked with the thin-arcs approximation without having to use the exact formula at all.

2.5. Stellar limb darkening

The most convenient way to treat limb-darkening effects is to decompose the source (assumed to be a disk) into N concentric annuli of inner and outer radii $\rho_{k-1} < \rho_k$ ($1 \leq k \leq N$) of constant surface brightness I_k , with $\rho_0 = 0$ and $\rho_N = \rho$. The visibility is then simply calculated as

$$\Phi_{\mu l} = \sum_{k=1}^N I_k (\Phi_{\mu l, k} - \Phi_{\mu l, k-1}), \quad (39)$$

where $\Phi_{\mu l, k}$ is computed for a source of radius ρ_k (or equivalently for the thin-arcs approximation, $\eta_{1, k}$, with $\eta_{1, 0} = 0$ and $\eta_{1, N} = \eta_1$). As limb-darkening affects the border of the disk of the source star, it will affect the ends of the arc-shaped images and will contribute as a correction only to the visibility.

In any case, a linear limb-darkening law will always provide a suitable description of the source's limb darkening. Adopting the (microlensing) convention that the limb-darkening law is normalised to total unit flux yields $I_k = 1 - \Gamma \left(1 - \frac{3}{2} (1 - r_k^2)^{1/2}\right)$, where Γ is the linear limb-darkening coefficient ($0 \leq \Gamma \leq 1$), and where $r_k = \rho_k/\rho = \eta_{1, k}/\eta_1$. The coefficient Γ is related to the more usual coefficient a by $a = 3\Gamma/(2 + \Gamma)$. The choice of the particular set of values ρ_k (or $\eta_{1, k}$) can be optimised to minimise N (e.g. with a linear sampling of I_k between its maximum and minimum values from centre to limb, respectively $(1 + \Gamma/2)$ and $(1 - \Gamma)$).

3. Application

3.1. Examples and discussion

Typical examples of visibilities ($|V_E|^2$ and $\phi = \arg V_E$) are shown in Figs. 6 to 11. All the figures were calculated for the same value of $\rho = 0.03$, slightly above the typical values to challenge the approximations derived in the previous sections. From Figure 6 to Figure 10 the distance of the source to the lens is decreased from $u_1 = 0.6$ to 0.032, and Figure 11 is a perfect Einstein ring ($u_1 = 0$). For each figure the upper panels show, on the left, the positions and shapes of the source and the images with the lens in the centre and, on the right, a three-dimensional view of the squared visibility in the Einstein $u_E v_E$ -plane. The middle panels show the squared visibility $|V_E|^2$ (left plot) and the phase ϕ (right plot). The bottom panels show the difference in squared visibility between either the point-source approximation (left) or the thin arcs approximation (right) and the exact calculation. For reference, the colour scale for these plots is set to saturate at $\Delta|V_E|^2 \pm 0.1$ (negative values in blue, positive in red) as they are typical minimum instrumental values of error bars on $|V_E|^2$.

For relatively large source-lens separations, such as $u_1 = 0.6$ in Figure 6, the images are just slightly elongated, and the point source provides a good approximation to the visibility. The minimum squared visibility differs from 0 and the phase spans a range of values because the two images have different magnifications. The thin-arcs approximation does not provide a good approximation in that case. When $u_1 = 0.3$ (Figure 7), the point-source approximation still holds for typical (u_E, v_E) values probed by the interferometer (data points expected at best between the two dashed circles), and the thin-arcs approximation starts to provide a fair approximation within the inner dashed circle.

When $u_1 \lesssim 0.2$ (peak point-source magnification of about 5), the situation is reversed, as seen in Figure 8 for $u_1 = 0.1$. The thin-arcs approximation now provides a very good approximation to the squared visibility (error $\leq 10^{-2}$) even outside the outer dashed circle. The point-source approximation is no longer a suitable model. In Figure 9 ($u_1 = 0.05$) and Figure 10 ($u_1 = 0.032$), the squared visibility progressively takes a circular shape, while the phase does not differ more than a few degrees from 0 or 180 deg. Finally, in Figure 11, the image is a perfect ring ($u_1 = 0$) and the thin-arcs approximation is as accurate as the exact calculation. The phase takes only the two values 0 and 180 deg.

In the situation described here ($\rho = 0.03$), the transition from the point-source to the thin-arcs approximation appears smooth for $|V_E|^2$, and unless we have to model interferometric data with very small error bars, it appears unnecessary to perform the exact calculation. The closure phase, however, still requires using the exact calculation, but its value is not expected to deviate more than a few degrees from 0. Finally, for smaller values of ρ , the thin-arcs approximation gives even better results for $|V_E|^2$, which justifies its use for a wide range of single-lens parameters.

3.2. Practical modelling

In this section we study possible strategies for fitting interferometric data to single-lens models, and we discuss suitable choices of model parameters for single-epoch or time-series data. In the following, we assume that the limb-darkening coefficient Γ of the source can be estimated independently (e.g. from a colour-magnitude diagram). The main parameters we discuss below are shown in Figure 5.

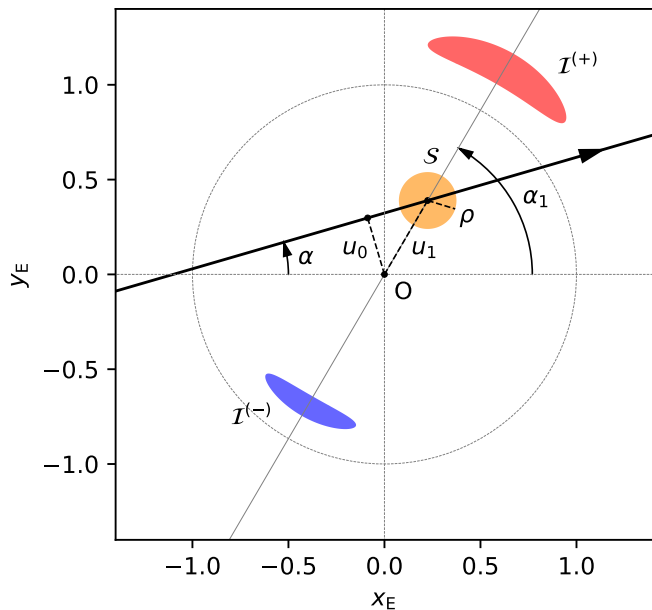


Fig. 5. Model parameters for a straight-line source-lens trajectory. The lens is the black dot in the centre, the source (unseen) is the orange disk S of radius ρ , and the red and blue arcs I^+ and I^- are the major and minor lensed images, respectively. The line joining the centre of the two images makes an angle α_1 with the x_E -axis, with the convention that the source centre lies at a distance $u_1 > 0$ from the lens, so that the major image is up for $\alpha_1 \in [0, \pi]$. The trajectory of the source with respect to the lens is shown as the thick black arrow. It makes an angle α with the x_E -axis, and u_0 is its signed impact parameter. As the source moves relative to the lens along the black arrow, the images rotate around the lens.

We first consider individual interferometric epochs. We first insist that the images are almost static during the time of an interferometric exposure (~ 10 mins). To compute the visibility, the point-source approximation requires u_1 as parameter, the exact formula (u_1, ρ), and the thin-arcs approximation η_1 . To fit the interferometric data, in all cases we must add α_1 as a parameter (orientation on the sky of the images) as well as θ_E (to convert Einstein units into radians). If the lens is luminous, an extra parameter must be added (Section 2.1): g_L when using the point-source approximation or the exact formula, and $g'_L = g_L \pi \rho^2 / u_1$ when using the thin-arcs approximation. In general, we expect g_L to be at least partly constrained by the light curve, so this parameter may not necessarily be fitted.

In the case of time-series interferometric observations, unless we independently obtain a precise information on the exact trajectory of source relative to the lens, we can assume that the source-lens trajectory is well approximated by a straight line. This approximation holds as long as the different epochs of observation span a relatively short interval of time, typically less than two weeks. The model parameter θ_E is again used as it gives the overall angular scale of the problem. When using the exact formula, the source radius ρ must be added as a parameter. Using the lens as a blend star adds another parameter, g_L or g'_L , as described in the previous paragraph. To describe the source-lens straight trajectory, we need to add the parameters α , the trajectory angle, and t_0 , a time origin (usually chosen to be the date at which the source is closest to the lens).

When using the exact formula or the point-source approximation, we also have to add in the list of parameters the Einstein timescale t_E (i.e. the time it takes for the source to travel θ_E) as well as u_0 , the minimum impact parameter of the source-lens trajectory. However, when using the thin-arcs approximation, u_0 is no longer a convenient parameter: if for every individual epoch only $\eta_1 = \rho/u_1$ can be measured, then (from Thales' theorem) only $\eta_0 \equiv \rho/u_0$ can be used as a parameter of the model. Similarly, t_E cannot be determined individually, as a trajectory with a higher value of u_0 implies a slower moving source (i.e. a higher value of t_E) for (almost) the same shape and location of the images; more precisely, the time Δt it takes for the source to travel between two epochs of observation is $\Delta t \propto u_0 t_E$, which means the product $p = u_0 t_E$ is constant. Hence, in principle p could be used as a model parameter, but in practice it appears more convenient to use the source radius crossing time, $t_* \equiv \rho t_E$, as it is the product of the two constant quantities $\eta_0 \times u_0 t_E$, and a classical parameter in microlensing modelling.

4. Summary and perspectives

In this work we first reviewed the main concepts and general formulae of interferometric microlensing, and detailed the equations useful for treating the case of a single lens. We recalled the well-known visibility formula for a point source, and then treated the case of an extended source, for which we proposed a new approach for the calculation of the visibility, allowing a robust and numerically efficient calculation.

This formalism allowed us to establish a new approximation, which we called the thin-arcs approximation, and which applies to microlensing events of medium or higher magnification observed around the peak (i.e. a large fraction of potential observational targets). We demonstrated that the computation time using this approximation is six to ten times faster than with the exact formula, and applies over a wide range of lens-source separations. It even turns out that a direct transition from the point-source to the thin-arcs approximations is possible in many situations, without having to calculate the visibility with the exact formula.

Accurate models and reliable numerical methods are of particular importance as the number of targets is expected to increase significantly in the near future. Based on a four years of statistics of microlensing events alerted by the OGLE collaboration (2011–2014, about 7000 events), Cassan & Ranc (2016) found that the number of potential interferometric targets N scales as $\sim 10^{0.4 \times \Delta m_K}$ with the event's peak magnitude m_K (obtained from a linear regression of the event's count, right panel of Figure 3 in Cassan & Ranc 2016); in other words, a gain in ~ 2.4 magnitudes in the instrument sensitivity results in about ten times more potential microlensing targets. Pushing the limiting magnitude of current or new-generation interferometers will therefore have a huge impact on the field.

Until recently, interferometric facilities suffered from a lack of sensitivity, limiting the pool of observable microlensing targets to the very bright tip of the distribution. Observations like those obtained for Gaia19bld at the VLTI (peak magnitude of $H = 6.2$, just above the PIONIER instrument's limiting magnitude of $H = 7.5$, see Ext. Data. Figure 1 in Cassan et al. 2022) hence remained exceptional. However, the latest improvements in interferometric instruments are going to be a 'game-changer', in particular for the ESO GRAVITY instrument at the VLTI. The new dual-field wide mode now available for GRAVITY, which uses a close and brighter star in the vicinity of the target to push the limiting magnitude up to $K \sim 16$, will significantly increase

the number of potential microlensing targets in upcoming observing campaigns. The expectations are 10 to 30 targets per year (and perhaps more), instead of about 1 target per year with the previous set-up. In addition to pinpointing the masses of exoplanets discovered through microlensing, these observations will allow us, for the first time, to unambiguously find isolated stellar black holes, and measure their masses with an exquisite precision.

References

- Cassan, A. & Ranc, C. 2016, MNRAS, 458, 2074
Cassan, A., Ranc, C., Absil, O., et al. 2022, Nature Astronomy, 6, 121
Dalal, N. & Lane, B. F. 2003, ApJ, 589, 199
Delplancke, F., Górski, K. M., & Richichi, A. 2001, A&A, 375, 701
Dong, S., Mérand, A., Delplancke-Ströbele, F., et al. 2019, ApJ, 871, 70
Einstein, A. 1936, Sci, 84, 506
Gould, A. 2000, ApJ, 535, 928
Paczynski, B. 1986, ApJ, 304, 1
Rattenbury, N. J. & Mao, S. 2006, MNRAS, 365, 792
Yoo, J., DePoy, D. L., Gal-Yam, A., et al. 2004, ApJ, 603, 139

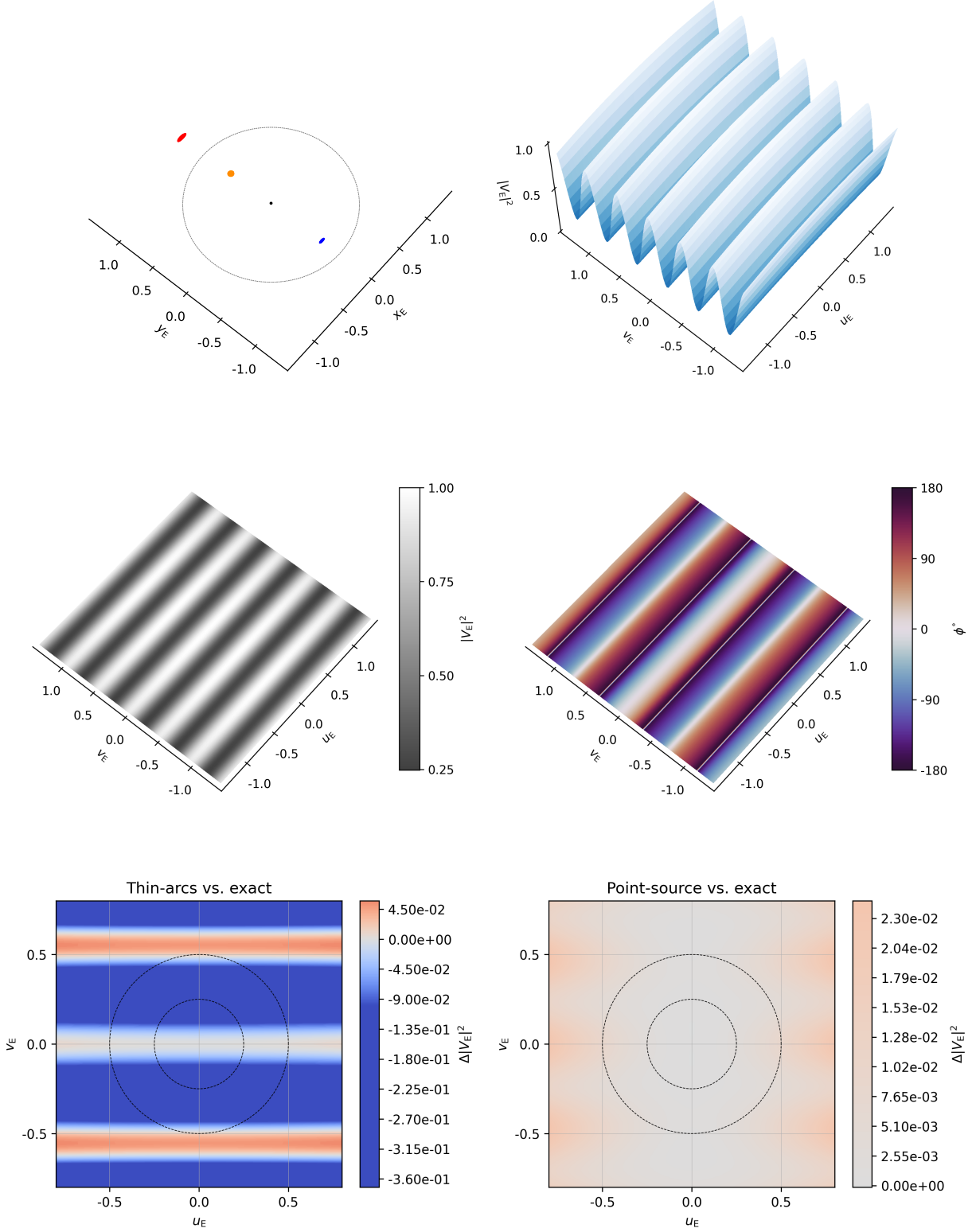


Fig. 6. Plots for $\rho = 0.03$ and $u_1 = 0.6$. *Upper panels:* Shown in the plot on the left are the lens (black dot in the centre), the (unseen) extended source (orange disk), and its two lensed images (red and blue arc-shaped images), displayed in (x_E, y_E) coordinates which are normalised by the angular Einstein ring radius θ_E . The plot on the right displays a three-dimensional view of the squared visibility $|V_E|^2$ in the Einstein $u_E v_E$ -plane, normalised by θ_E^{-1} . *Middle panels:* Shown in the plot on the left is a contour plot of $|V_E|^2$, while the plot on the right shows the phase of the complex visibility $\phi = \arg V_E$ (the thin white line is a visualisation artefact when ϕ jumps from $-\pi$ to π , or vice versa). *Lower panels:* Difference in squared visibility $\Delta|V_E|^2$ between either the point-source (left) or the thin-arcs (right) approximation and the exact calculation. The colours saturate for a difference of ± 0.1 . The inner dashed circle marks the typical angular resolution (radius 0.25), and the outer circle (radius 0.5) twice the typical resolution.

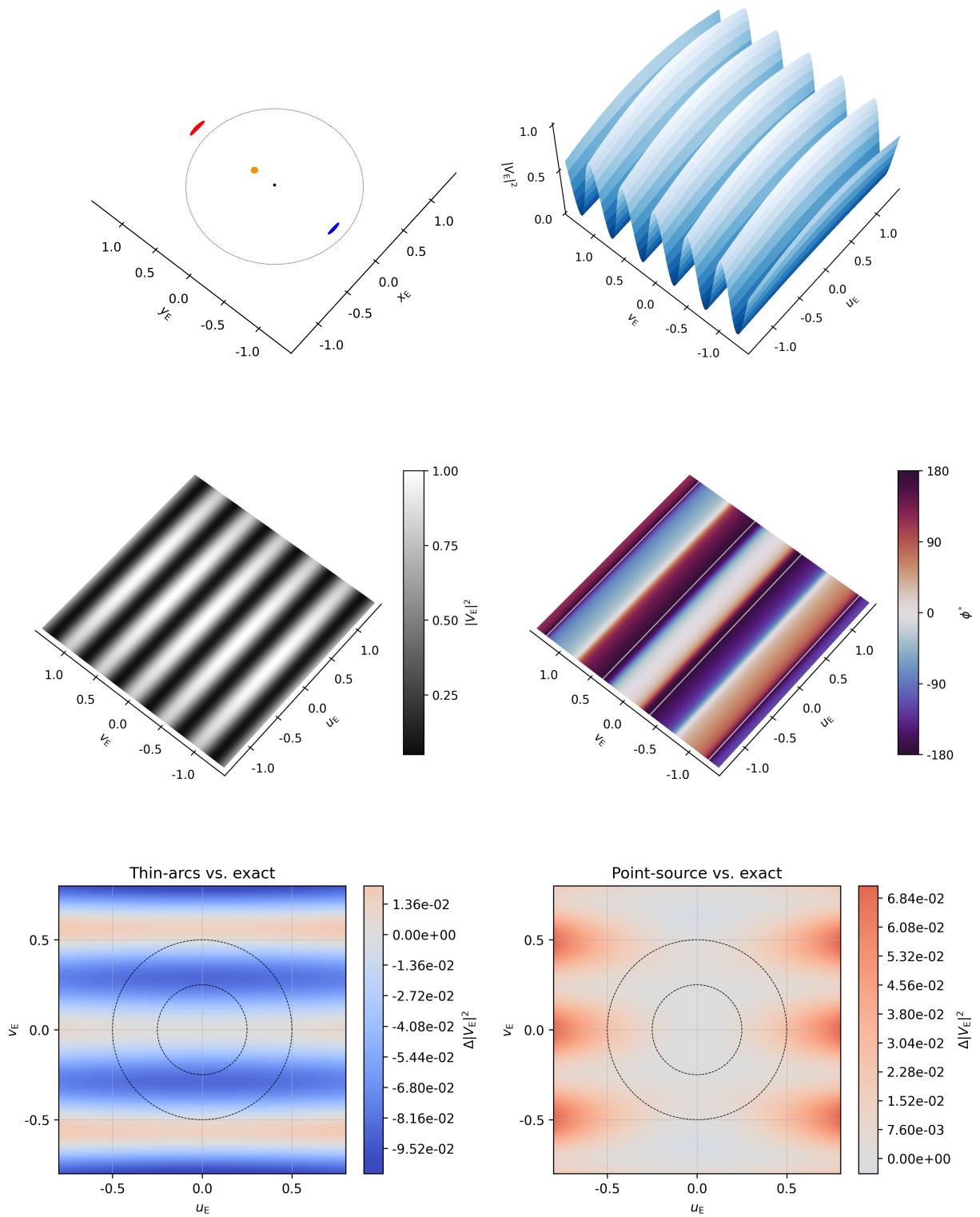


Fig. 7. Same as Figure 6, but for $u_1 = 0.3$.

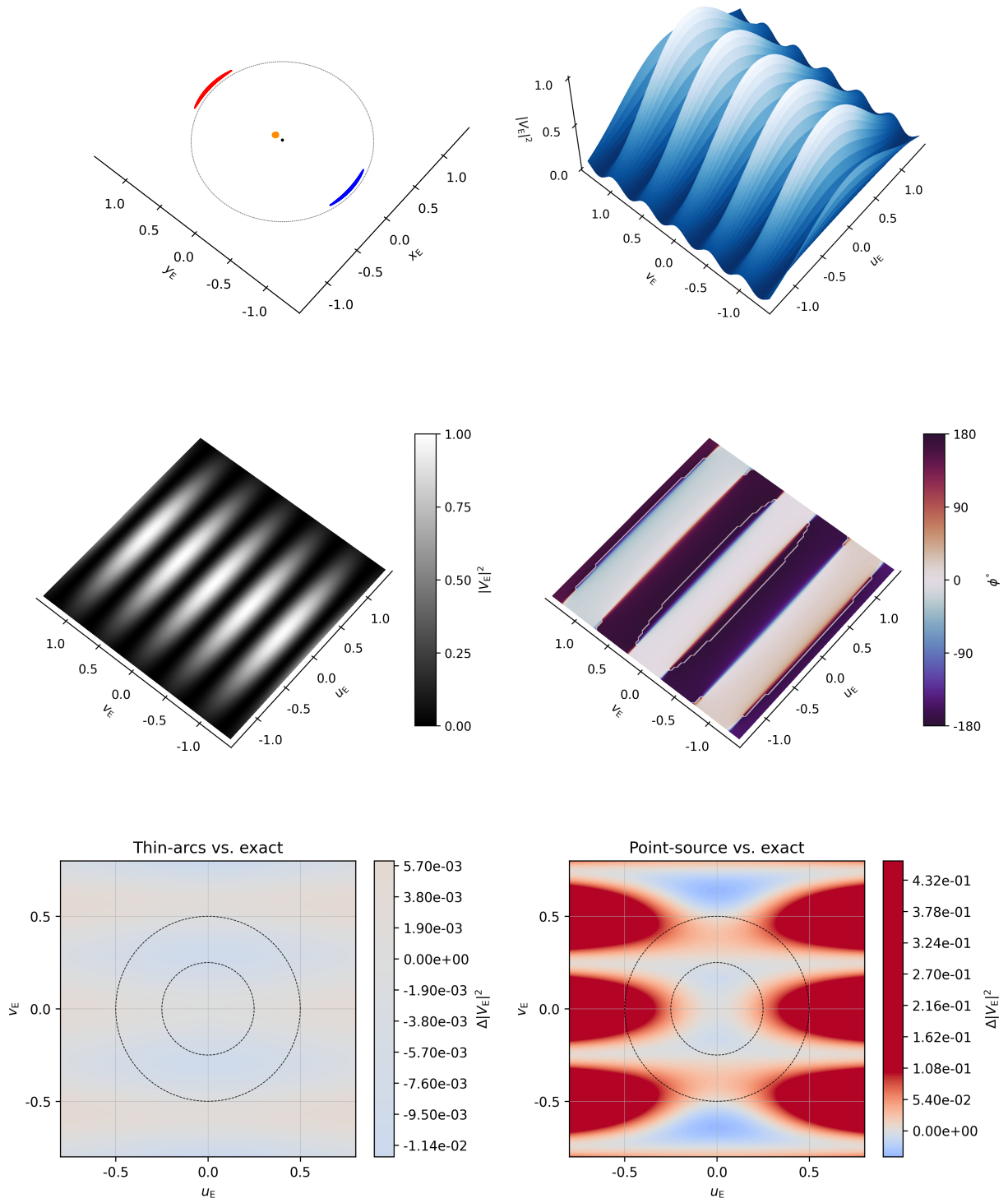


Fig. 8. Same as Figure 6, but for $u_1 = 0.1$.

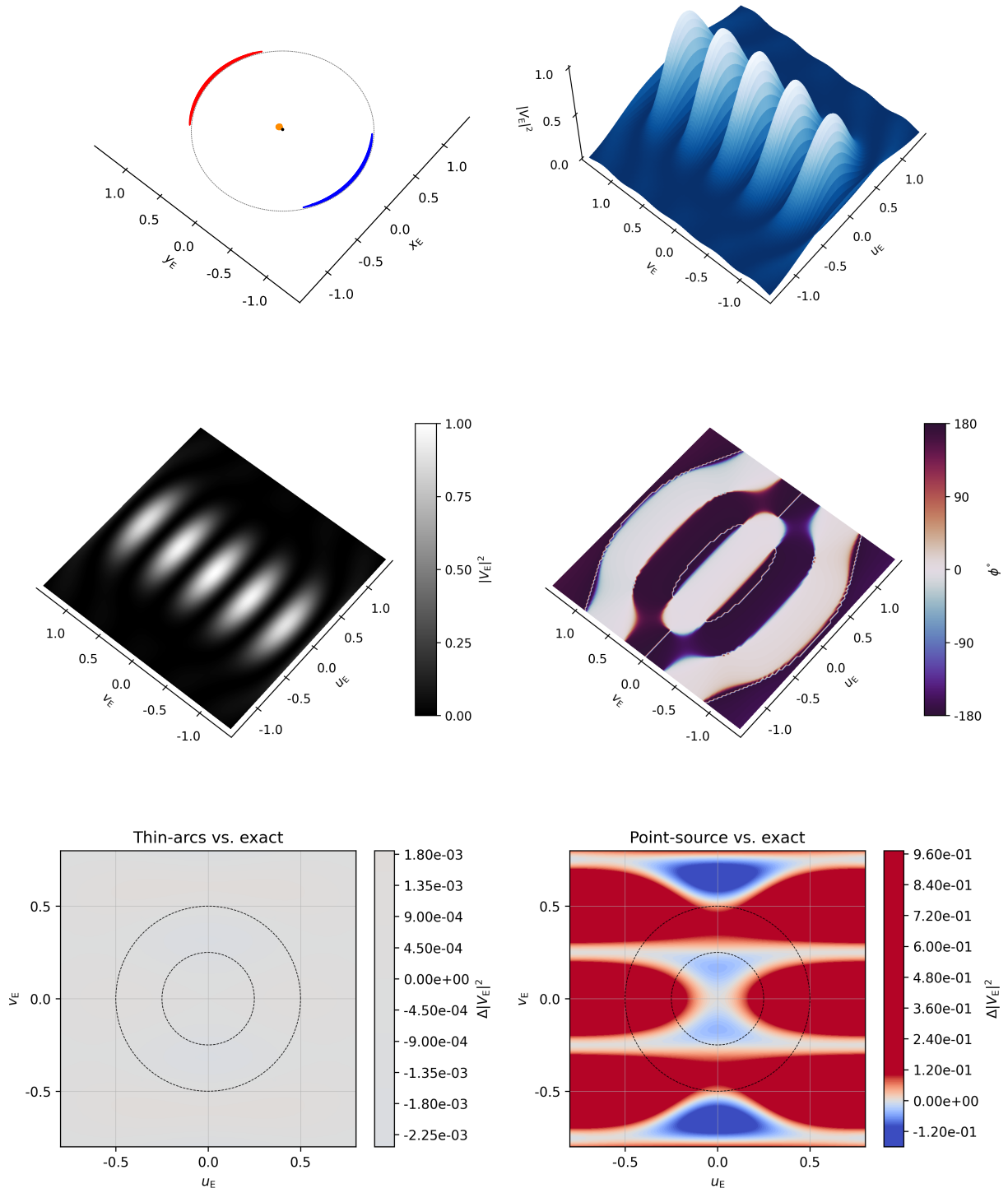


Fig. 9. Same as Figure 6, but for $u_1 = 0.05$.

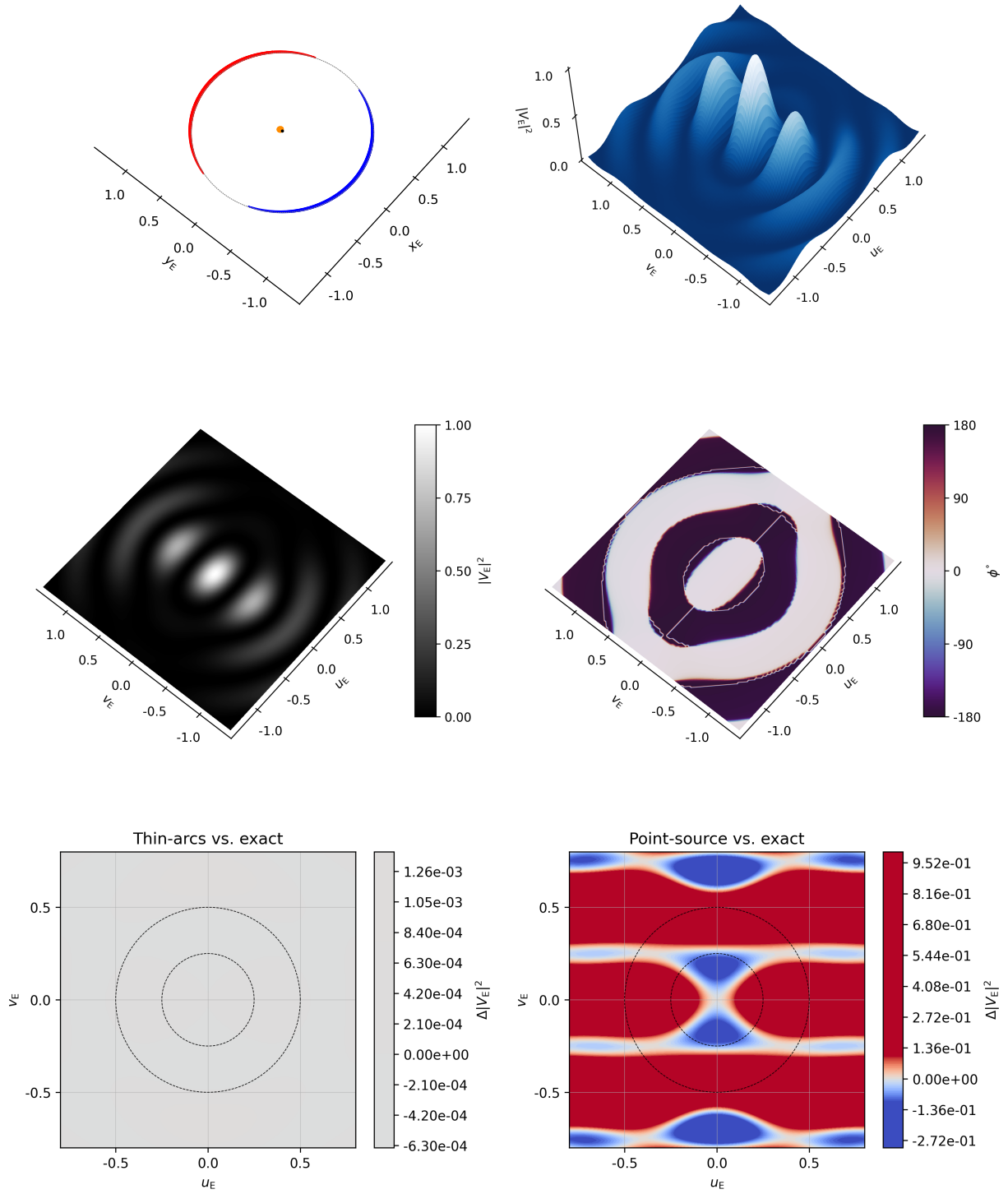


Fig. 10. Same as Figure 6, but for $u_1 = 0.032$.

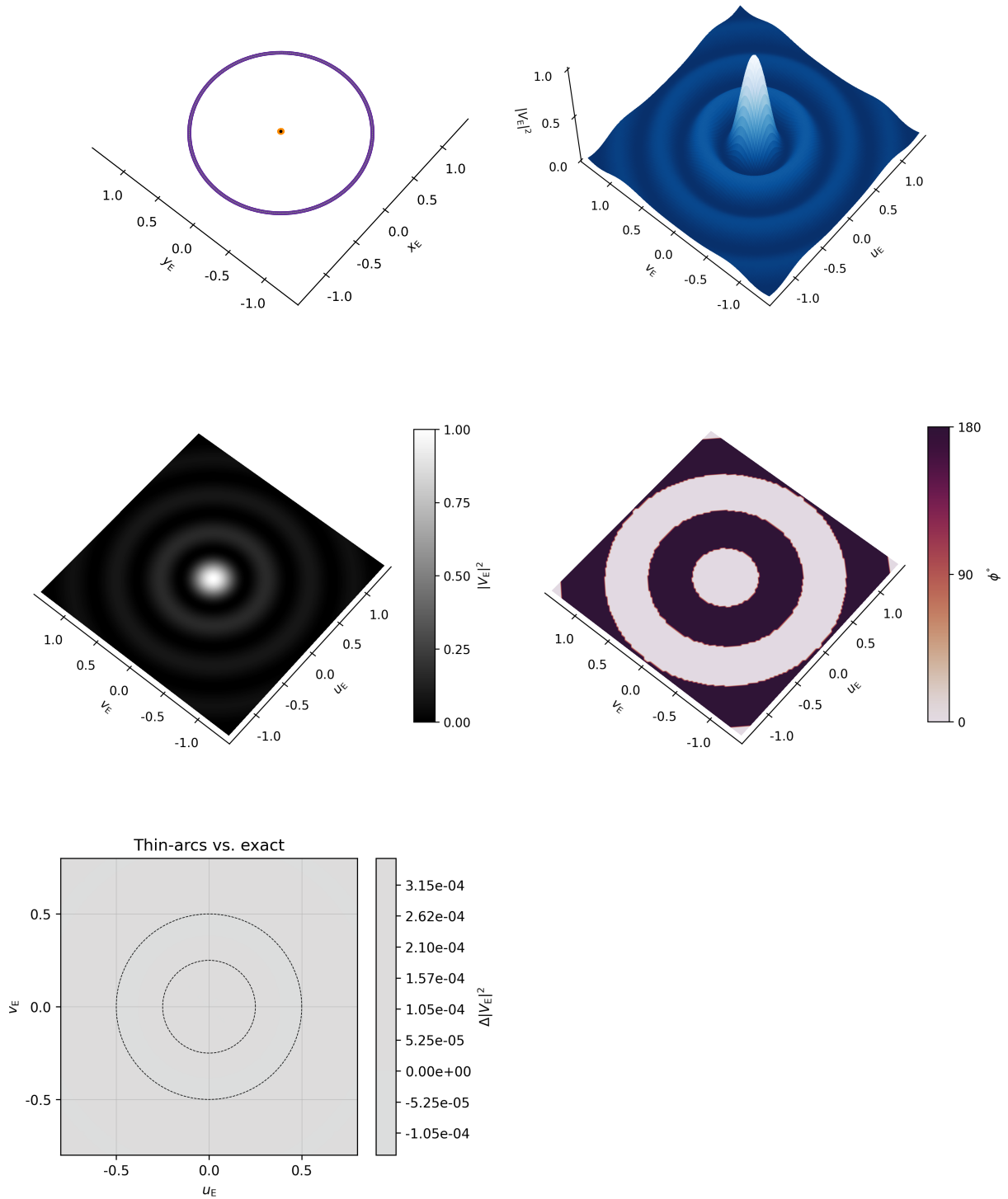


Fig. 11. Same as Figure 6, but for $u_1 = 0$. In this case the point-source approximation yields a circle instead of two point-like images and is not shown here.